Chapter 3

Enhanced Dielectrics, Ferroelectric and Optical Properties of Lithium Niobate for High Temperature Applications Using Potassium Oxide (K_2O) Additive

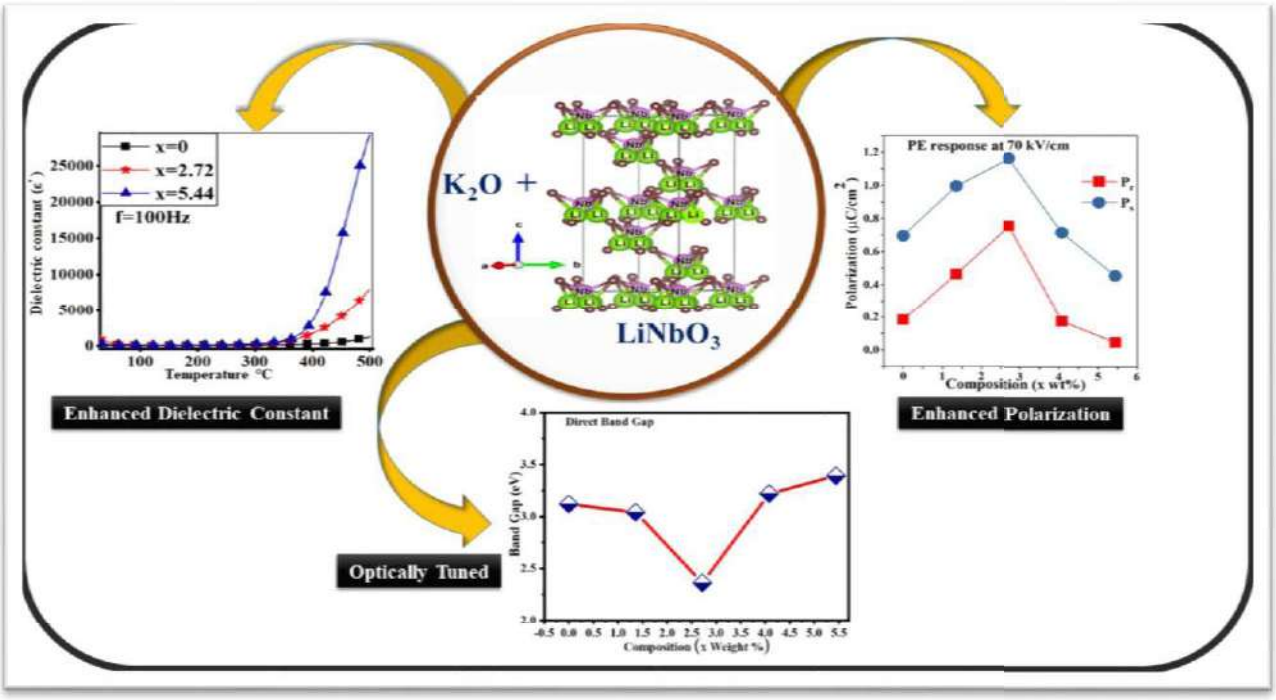

Chapter 3. Enhanced Dielectrics, Ferroelectric and Optical Properties of Lithium Niobate for High Temperature Applications Using Potassium Oxide (K_2O) Additive

3.1 Introduction:

In Chapter 1, we discussed about the significance of environmentally friendly electrical energy storage materials for various applications. In recent years, extensive research has been conducted to explore non-lead, non-bismuth-based, environmentally sustainable electrical energy storage materials suitable for high-temperature applications. In the case of $LiNbO_3$, most of the research has focused on single crystals form. However, the existing literature also provides information on bulk $LiNbO_3$ ceramic materials. Our literature survey has revealed several recent publications on $LiNbO_3$ ceramic-based materials, which is throwing light on the path of future research in response to rising demand for energy-related solutions. Some important conclusions from these recent publications are discussed as follow.

D. Sugak at el published a research article on Pr^{3+} doped $LiNbO_3$, $LiNbO_3$:Mg, $LiTaO_3$ Nanopowders for Mechanosynthesis, Structure, and Photoluminescent Properties. In the synthesis process of the samples, two pressing modes were employed. In the first mode, heating was carried out in the presence of an electric field, while the second mode did not involve additional factors. The excitation and photoluminescence of praseodymium ions were investigated, and concluded that the method of sample preparation significantly influenced the properties. A higher relative photoluminescence intensity was observed for the sample pressed in the presence of both temperature and an electric field. This results could be attributed to the significant role played by the electric field for higher ordering of ferroelectric nanoparticles during the pressing process. The researchers also investigated the temperature dependence of the electrical conductivity of the $Li_{0.98}Pr_{0.02}NbO_3$ sample. They concluded that

the conductivity mechanism at higher temperatures is similar to that of $LiNbO_3$ single crystals, and this was attributed to the lithium conduction mechanism[1].

A study on the domain structure modulation of $LiNbO_3$ thin films using focused ion beam (FIB) technology was conducted by Y. Batra et al. and it was reported in an article. Scanning Kelvin probe microscopy (SKPM) and piezo response force microscopy (PFM) are two non-destructive techniques they were utilized to investigate these domains and assess their polarization characteristic. Using SKPM surface potential measurements and PR phase data, they concluded that the antiparallel polarization directions in nearby domains resulted in a surface potential differential of about 35 mV between the oppositely polarized domains [2].

In this chapter we have given the details study of synthesis of $LiNbO_3$ (LN) and K_2O added LN which is $LiNbO_3$ + x (wt%) K_2O, via solid state reaction method. There are various other methods like sol-gel method, co-precipitation method, electrochemical crystal growth, hydrothermal method, solid state reaction method, etc., that can be used for the preparation of samples. As compared to traditional synthesis rout, solid state reaction method eases the production of high pure samples at large quantity economically[3]. Although the solid-state reaction is very simple, this process is not entirely satisfactory in case of $LiNbO_3$ as the high calcined temperature changes the molar ratio of Li/Nb due to the high evaporating pressure of lithium. The evaporation of lithium ions causes the niobium ions to change the valence to balance the chemical formula[4]**.** Dielectric properties of LN are enhanced by the addition of potassium oxide are rarely reported and this report opens a path for large scale production of high temperature Lithium Niobate based dielectric materials with high dielectric properties with low dielectric loss. The objective of present study in this research paper are, (i) to synthesis Potassium Oxide (K_2O) added LN via solid state reaction route and (ii) to study the

structural and dielectric properties with varying frequencies and temperature (iii) study and analysis of ferroelectric properties of prepared material at room temperature (iv) Study and analysis of the optical and photoluminescence properties. This work focuses on the development of dielectric material with low dielectric loss for high temperature applications.

The objectives of this present research work is study and examine of an environmental friendly sustainable energy storage ceramic material for the high temperature applications at low cost. The limitation of this present work is after a 5.44 wt% addition of K_2O the secondary phases might be arises which can alter the properties also.

The synthesized samples were characterized for phase, crystallinity and particle size through powder XRD and SEM. Le-Bail fitting also done to find out crystallographic parameters. For electrical properties investigation we have done Polarization electric field loop characterization, Dielectrics measurements (Permittivity and Tangent loss)**.** To investigate the thermal stability of prepared samples TGA characterizations also performed up to higher temperature. Improvement of sintering properties of LN pellets by lowering sintering temperature also presented. The result of this research work is compared with some previous research works and their results. The crystal structure of LiNbO3 shown in the Figure 3.1, which is drawn by using lattice parameters through VESTA software.

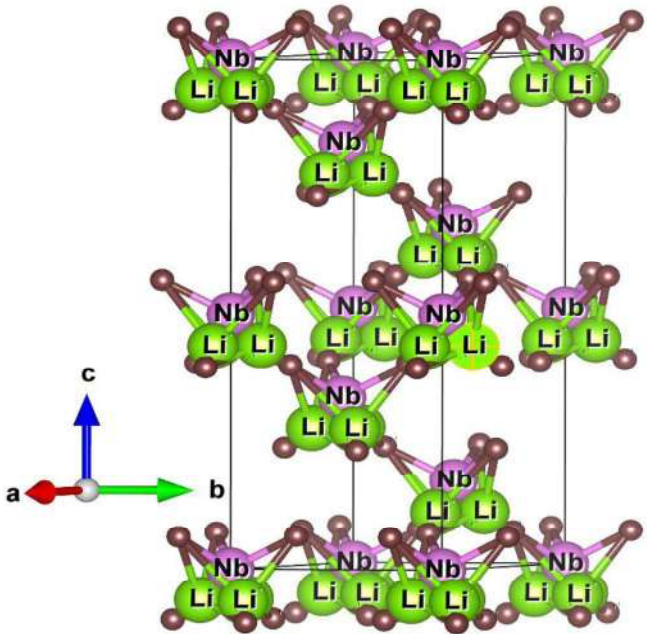

Figure 3.1: Schematic unit cell of the pure lithium niobate drawn by VESTA software using the structural parameters obtained from Rietveld structure refinement.

3.2 Experimental:

The initial reactant salts were lithium carbonate Li_2CO_3 (S. M. Chemicals, 98.50%), niobium pentoxide Nb_2O_5 (Sigma Aldrich, 99.99% purity), potassium carbonate K_2CO_3 (Sigma Aldrich, 99.00%). Pure Lithium niobate and potassium oxide added lithium niobate samples were synthesized via solid-state high-energy ball milling method using Retsch PM400 MA ball mill. Powder mixture of Li_2CO_3, Nb_2O_5 and K_2CO_3 were milled in high energy planetary ball mill using ethanol wet medium with milling speed of 300 rpm for 8 hours. After milling, powder was kept overnight for drying and then calcined at 750°C for 6-hour. For confirmation of perovskite phase formation calcined powder were characterized by Rigaku Miniflex X-ray diffractometer with CuK_α radiation. Calcined powders were pressed in to pellets of 10 mm diameter and 1 mm thickness under 5 Ton pressure for 90 seconds using hydraulic press and PVA as a binder. The pressed pellets were kept at 550°C for 8 hours for

binder burn out. The pellets were sintered at 1050 ℃ for 6 hours with heating rate of 3 ℃/minute. For sintering, green pellets were kept at alumina disk covered with alumina crucible which was sealed with MgO powder[5], to provide close environment to avoid lithium oxide evaporation so that stoichiometry of the system is maintained. For XRD characterization, sintered samples were crushed into powders and annealed at 500 ℃ for 8 hours. Highly dense sintered pellets were used for electrical characterization after applying silver electrodes on both flat sides of pellets.

3.3 Characterizations:

The phase purity and structural information of synthesized samples of pure and Potassium Oxide added Lithium Niobate were characterized by using Rigaku Miniflex X-Ray diffractometer with Cu K_α radiation (1.5406 Å). The measurement was performed at a sweeping rate of 3 degrees/minute and the X-Ray machine was operated at 40 kV and 15 mA. ICDD data base were used for phase determination, peak reflection assignments and to analyze variations in peak positions and intensities. The crystallographic lattice parameters were obtained by Lebail profile matching refinement of XRD data using Fullprof Suite software. Utilizing an X-ray Photoelectron Spectrometer (XPS) system, X-ray photoelectron spectroscopy characterization was done. The morphological analysis of samples was investigated by Scanning electron microscope [SEM] (JCM-6000 Plus BenchTop Sem Neoscope, JEOL Asia PTE Ltd). ImageJ software was utilized to determine the average grain size of the sintered pellets from SEM micrographs. An impedance analyzer (Keysight E4990A) was used to measure the dielectric characteristics at frequencies of 1 kHz, 100 kHz, and 1 MHz and temperatures ranging from room temperature to 500°C. Ferroelectric characteristics were examined with a ferroelectric tester developed by Radiant Technology

(Precision Premier-II) while the sample was kept at room temperature. The FTIR analysis of the functional group as well as the purity of the produced sample were performed using Nicolet Summit FTIR Spectrometers. The absorbance properties of the samples were measured using a JASCO V-650 UV-visible Spectro-photometer in the spectral range of 200-800 nm and at a scan rate of 2 nm/s at room temperature. The direct band gap was also calculated using the Tauc Plot equation. The weight loss with temperature and activation energy of the synthesized samples were investigated by thermo-gravimetric analysis which performed by Shimadzu TGA-50. The excitation and emission spectra of the annealed powders of the produced samples were measured in the 350–700 nm region using a fluorescence spectrometer (Hitachi F-4600).

3.4 Results and discussion:

3.4.1 Crystal structure analysis

In the Figure. 3.2(a-b), the X-ray diffraction pattern of $LiNbO_3$ ceramic is shown, the **Figure 3.2(a**) is depicted to the calcined powder of the $LiNbO_3$ ceramic where the calcination temperature was 750 °C for 6 hours and **Figure 2(b)** is depicted to the powder of sintered sample. When the $LiNbO_3$ is calcined at 750 °C there is an impurity peak is arising which is shown in the **Figure 2(a),** that peak eliminated when the same $LiNbO_3$ pellet is sintered at 1050 °C.

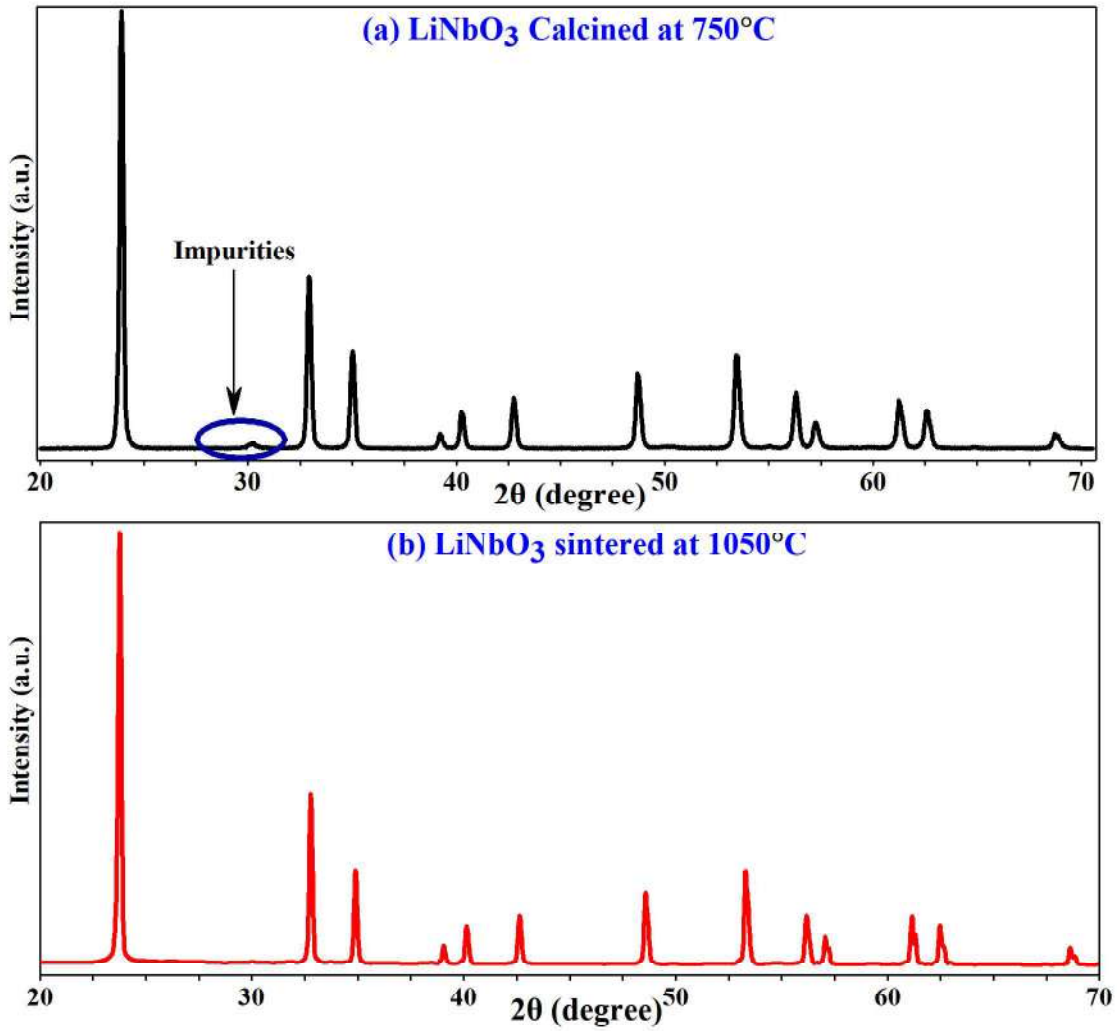

Figure 3.2(a-b): X-Ray diffraction pattern of $LiNbO_3$ (a) for Calcined powder at 750 °C (b) for sintered pellet at 1050 °C.

The **Figure 3.3,** shows a comparison of X-ray diffraction (XRD) patterns of lithium niobate (LN) with different weight percent of potassium oxide (K_2O) additive for the samples sintered at 1050°C for 6 hours. It was found that pure perovskite phase similar to LN with rhombohedral structure is obtained for lower compositions but secondary phase of niobium oxide appears when K_2O content exceeded to 4.08 wt% and above for the same sintering temperature of samples. The peaks corresponding to LN type rhombohedral structure The confirmation of XRD pattern peaks is done ICSD collection code 201274.

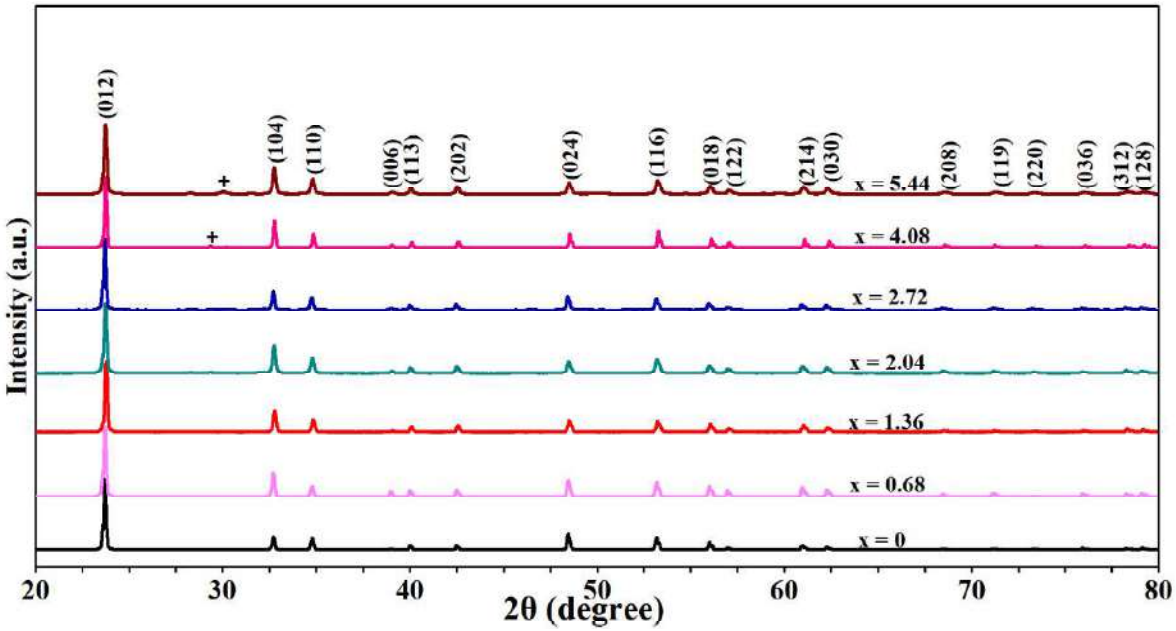

Figure 3.3: X-Ray diffraction pattern of $LiNbO_3$ + x (wt%)K_2O with varying composition of x.

In order to confirm the crystal structure and determine the lattice parameters and the unit cell volume, Le Bail profile matching refinement was performed to fit the XRD data using FullProf Suite. The Le-Bail profile matching technique essentially accomplishes a comparable objective to the well-established Rietveld structure refinement methodology in the field of crystallography[6]. When the solution contains a lot of atoms and/or certain lighter atoms, such H, Li, Be, and B, it can be effectively used to identify or refine the crystal structure lattice parameters[7–10] **30-33**. **Figure 3.4(a-e)** demonstrate very good Le Bail refinement fits for the XRD patterns of the compositions with x=0, 1.36, 2.72, 4.08 and 5.44. Thus, the Le Bail analysis of all the compositions confirms that their crystal structure is rhombohedral with R3c space group. The refined lattice parameters obtained from the Le Bail refinement fits are listed in **Table 1** for all the samples. As evident from this table there is negligible change in the lattice parameters while changing the content of K_2O additive.

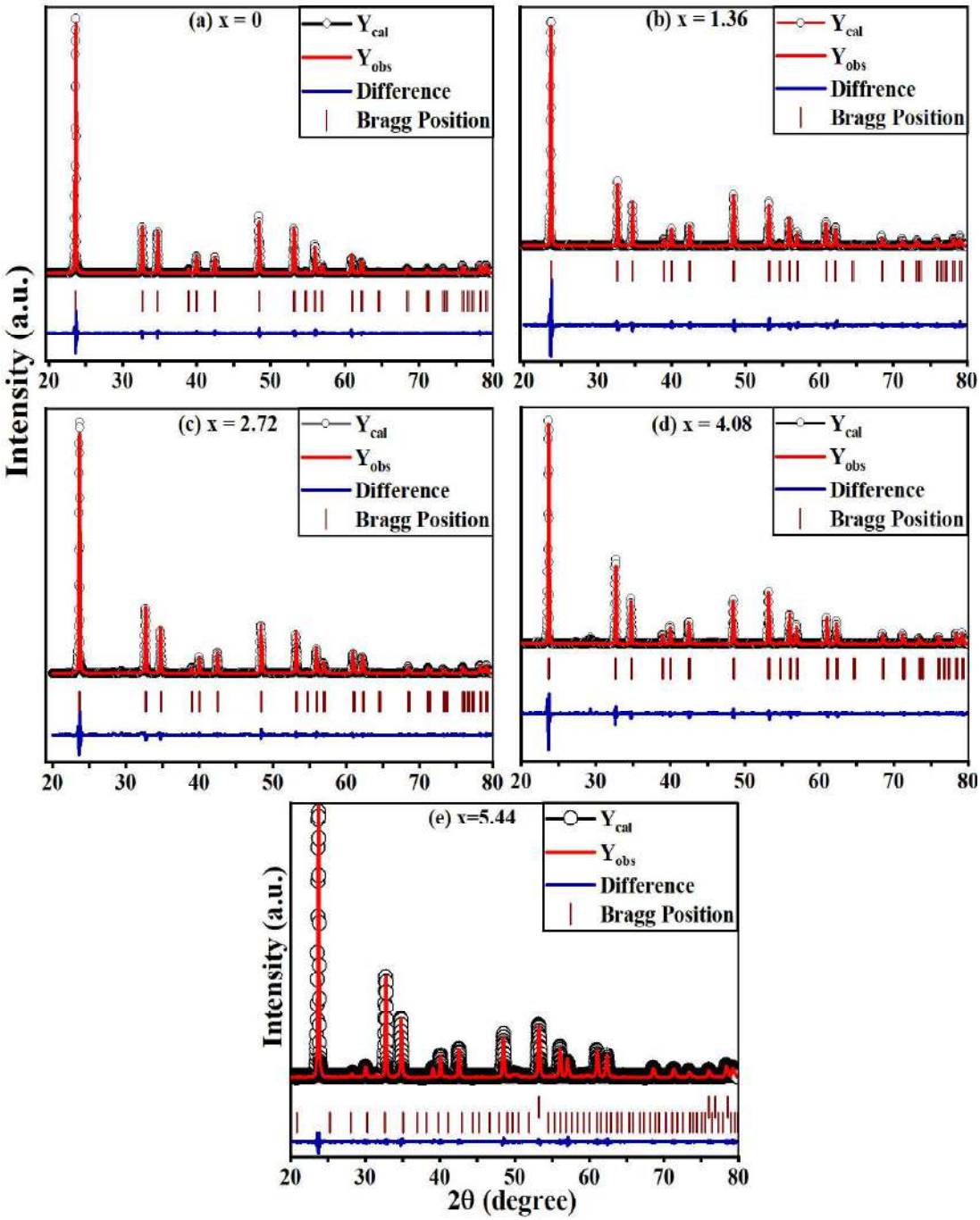

Figure 3.4: (a-e) Lebail structural Refinement fitting for LN + x (wt%)K_2O.

Table 3.1: Crystal lattice parameters and unit cell volume for various compositions of LN with K_2O additive, obtained from Le Bail refinement.

Compositions	a (Å)	b (Å)	c (Å)	Direct cell volume ($Å^3$)
x = 0	5.1631(5)	5.1631(5)	13.8712(7)	320.237(1)
x = 1.36	5.1699(5)	5.16999(5)	13.8552(1)	320.714(1)
x = 2.72	5.1640(5)	5.1640(5)	13.8633(3)	320.170(6)
x = 4.08	5.1587(9)	5.1587(9)	13.8655(1)	319.554(5)
x = 5.44	5.1563(4)	5.1563(4)	13.8386(6)	320.649(1)

3.4.2 Morphological analysis:

The **Figure 3.5(a-c)** depicted for the morphological analysis of the calcined powder of the LN + x (wt%)K_2O ceramic for the composition x = 0,2.72 and 5.44. In the **Figure 3.5(d-f)** the particle size distribution has been shown for the respective composition of x. The average particle size for the calcined LN + x (wt%)K_2O ceramic powder ranges between 269 nm to 285 nm.

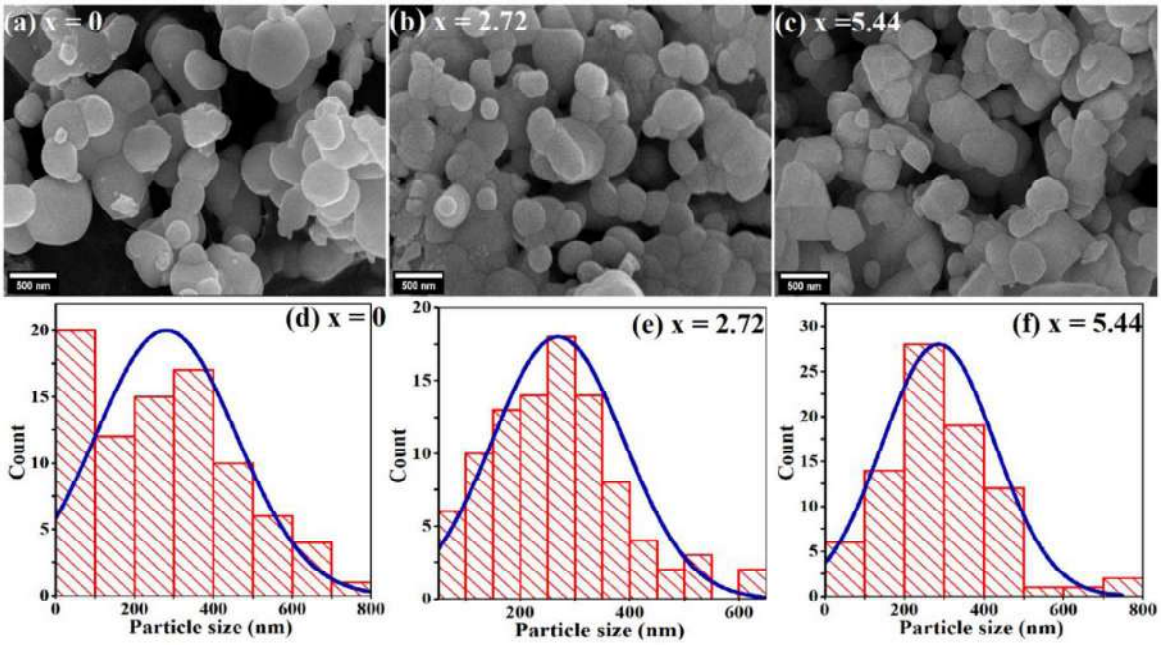

Figure 3.5:(a-f) Scanning electron microscopic images of LN + x (wt%)K_2O calcined powder, **(d-f)** Particle size distribution.

In the **Figure 3.6(a-c)** Energy-Dispersive X-ray Spectroscopy (EDS) spectra of LN + x (wt%)K_2O calcined powder has been shown for the composition x = 0,2.72 and 5.4, and each elemental composition for the respective composition is also mention in those figures through a table. Through this results it is observed that the all elements are present in the prepared LN + x (wt%)K_2O ceramic system for analysed compositions.

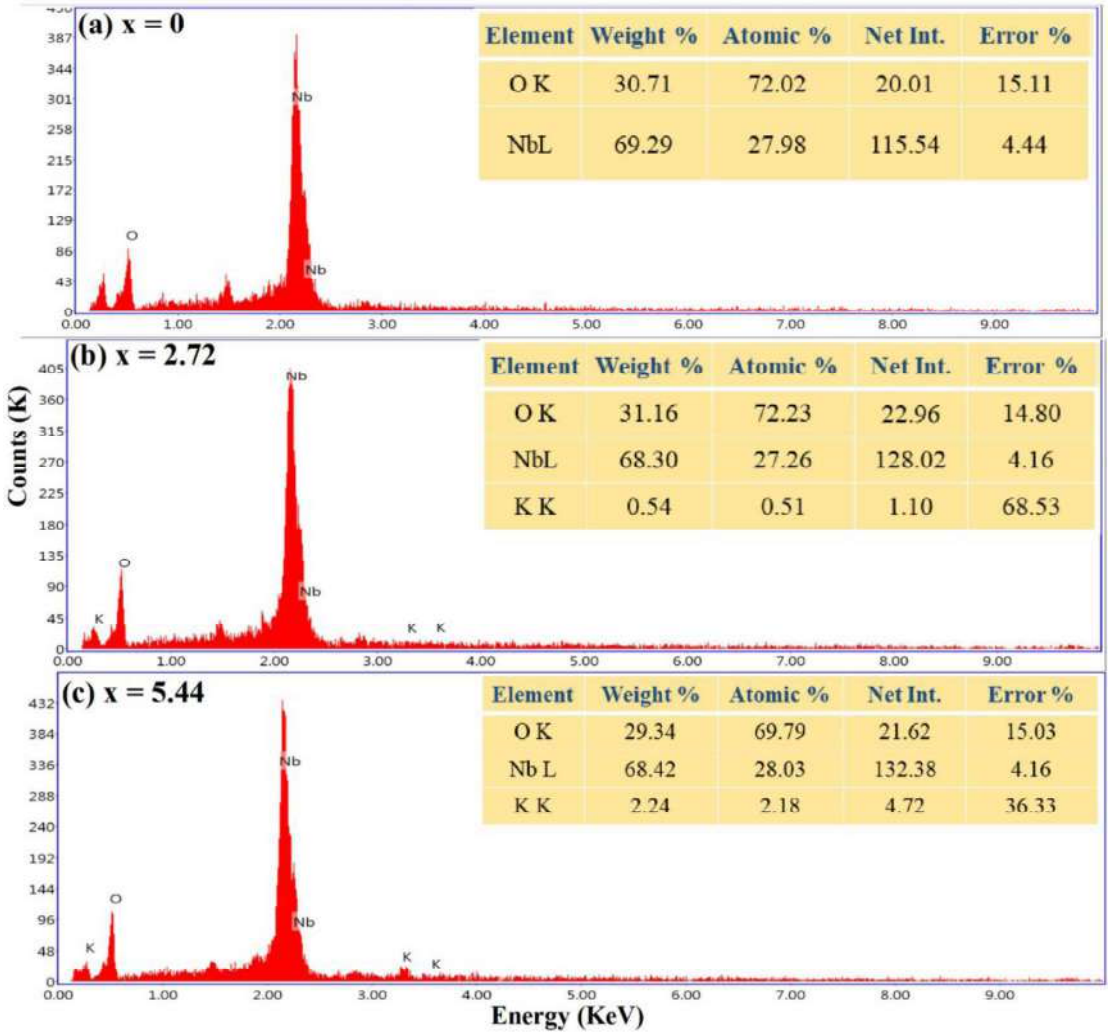

Figure 3.6: (a-c) Energy-Dispersive X-ray Spectroscopy (EDS) spectra of LN + x (wt%)K_2O calcined powder.

The **Figure 3.7(a-e)** depicts scanning electron microscopy (SEM) images of different compositions. The average grain sizes for different compositions were determined from the micrographs with the help of ImageJ software [11–14]. The corresponding histograms are plotted in the insets to respective micrographs in **Figure 3.7(a-e)**. It has been noticed that pure LN as well as K_2O added LN exhibit good crystallinity and a well-defined regular grains. The grain morphology has been observed to be clear and distinct, with clearly defined grain boundaries and an average grain size of roughly 12.5 µm for pure LN while after addition of

K_2O the grain sizes has reduced. The average grain sizes for various LN compositions with K_2O additive are 4.9 μm for 1.36 wt%; 3.6 μm for 2.72 wt%; 5.7 μm for 4.08 wt% and 7.4 μm for 5.44 wt%, respectively. The **Figure 3.7(f)** depicts the bar diagram comparison of average grain sizes for various compositions. The grain size initially decreases with K_2O addition and then increases for higher compositions. The **Figure 3.8(a-c)** depicts the results of elemental analysis on three compositions using energy dispersive spectroscopy (EDS). The EDS spectrum for the pure LN as well as with 2.72 wt% and 5.44 wt% K_2O additive are shown in **Figure 3.5(a), 5(b)** and 5**(c)** respectively. Since lithium has very low atomic number it cannot be detected by the EDS studies. The EDS peaks corresponding to the remaining elements Nb, K and O are seen in **Figure 3.8**. The **Table 2** lists the concentration of these elements for pure LN and with 2.72 wt% and 5.44 wt% K_2O additive as determined from EDS studies. The atomic percentages of Nb and O for pure LN matches well with the expected nominal values. The oxygen is underestimated for 5.44 wt% K_2O additive composition, perhaps due to larger oxygen vacancies. The **Table 3,** lists the density of sintered LN with various concentrations of K_2O additive. It is clearly seen that the densification is significantly improved by using K_2O additive.

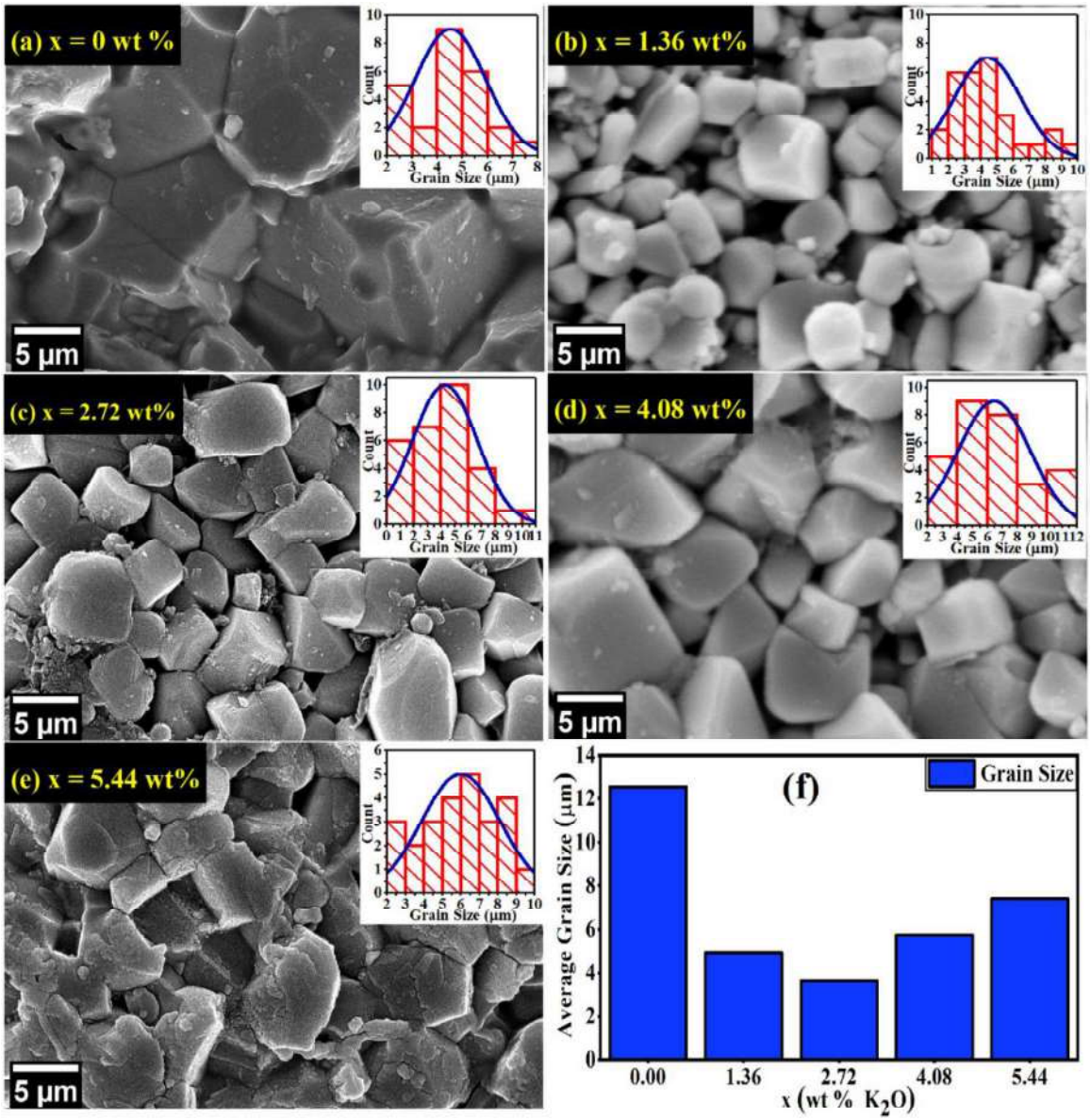

Figure 3.7(a-f): (a-e) Scanning electron microscopic images of $LiNbO_3$ with different concentration of K_2O additive and histogram of the grain sizes (inset), **(f)** Bar diagram comparison of average grain sizes for various compositions.

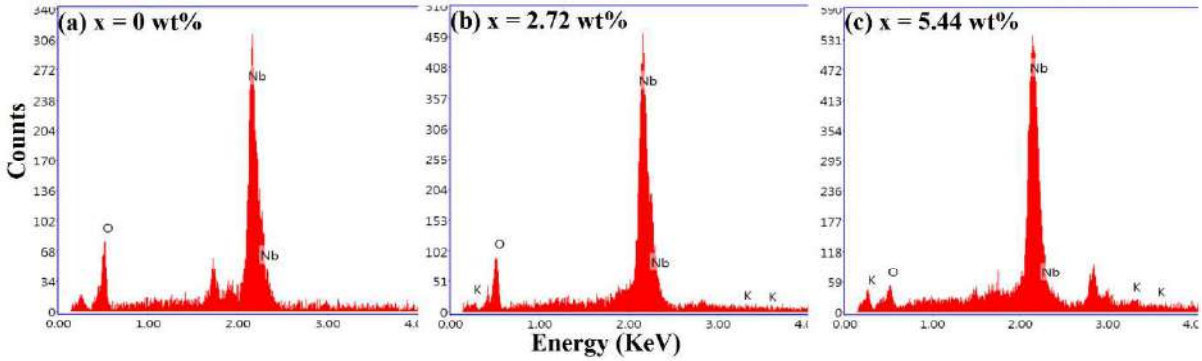

Figure 3.8: (a-c) EDS Spectrum analysis of $LiNbO_3$ with different concentration of K_2O additive.

Table 3.2: Percentage of elemental composition for pure LN and with 2.72 wt% and 5.44 wt% K_2O additive as determined from EDS studies.

Pure $LiNbO_3$		**LN with 2.72 wt% K_2O**	**LN with 5.44 wt% K_2O**
Element	**Atomic (%)**	**Atomic (%)**	**Atomic (%)**
O	74.11	69.61	51.68
Nb	25.89	29.66	45.36
K	0	0.73	2.96

Table. 3.3: Density of sintered LN with various concentration of K_2O additive.

Composition	**Density (g/cm^3)**
x = 0	**4.84**
x = 1.36	**5.04**
x = 2.72	**5.02**
x = 4.08	**4.99**
x = 5.44	**4.97**

3.4.3 X-ray Photoelectron Spectroscopy Study

We have used the XPS techniques to **analyze** the elemental composition and chemical valance state of different ions in our samples. The **Figure 3.9(a-c)** shows the XPS spectra of oxygen for pure LN, and with 2.72 wt% and 5.44 wt% K_2O additive concentration. It is observed that the O1s peak has two distinct components that can be de-convoluted into two peaks with binding energies of, 531.02 eV and 529.29 eV for pure LN; 532.27 eV and 529.41

eV for 2.72 wt% K_2O; and 531.71 eV and 529.42 eV for 5.44 wt% K_2O additive composition. The peaks at 529.29eV, 529.41eV and 529.42eV are attributed to the lattice oxygen[15]. The O1s peaks at 531.02 eV, 532.27 eV and 531.71 eV are satellite peaks and are observed because of physically adsorbed moisture in the system and also because of potassium oxide (K_2O) concentration in the system. Moisture absorption from the atmosphere is increased because potassium is hygroscopic in nature so that the satellite peaks of O1s is bigger and correspond to hydroxyl oxygen of the system[16,17]. The two XPS binding energy peaks for Nb 4S and Li 1S are shown in **Figure 3.9(d-f)** that are consistent with the previous reports of Steiner et al. [18]. The Nb 4S binding energy peak for the LN and LN with 2.72 wt% and 5.44 wt% K_2O additive concentrations are observed at 59.56 eV, 59.64 eV and 59.67 eV respectively. Similarly, Li 1S peaks are observed at 54.18 eV, 54.26 eV and 54.56 eV energies for the pure LN, 2.72 wt% and 5.44 wt% K_2O additive concentrations, respectively. The **Figure 3.9(d-f)** also show the chemical bonding of Li 1S with only one contribution at respective binding energies for the samples, and the detection of Li 1S peak with low intensities for the prepared samples at 54.18 eV, 54.26 eV and 54.56 eV also reveals the presence of residual lithium in crystal structure[19,20]. The **Figure 3.9(g-i)** depicts the Nb3d XPS spectra for pure LN, and LN with 2.72 wt% and 5.44 wt% K_2O additive concentration. The two peaks corresponding to the binding energies for Nb $3d_{3/2}$ and $Nb3d_{5/2}$ appear at 208.92 eV, 206.20 eV for pure LN, 209.15 eV, 206.37 eV for 2.72 wt% K_2O and 209.11 eV, 206.34 eV for 5.44 wt% K_2O additive concentration. The lower binding energy peak is attributed to Nb^{5+} oxidation state and Higher binding energy peak is attributed to Nb^{4+} oxidation state [21,22]. The **Figure 3.9(j-k)** confirm the presence of potassium in the prepared system as the two characteristic peaks for K^+ cations are seen for $2p_{3/2}$ and $2p_{1/2}$. The two

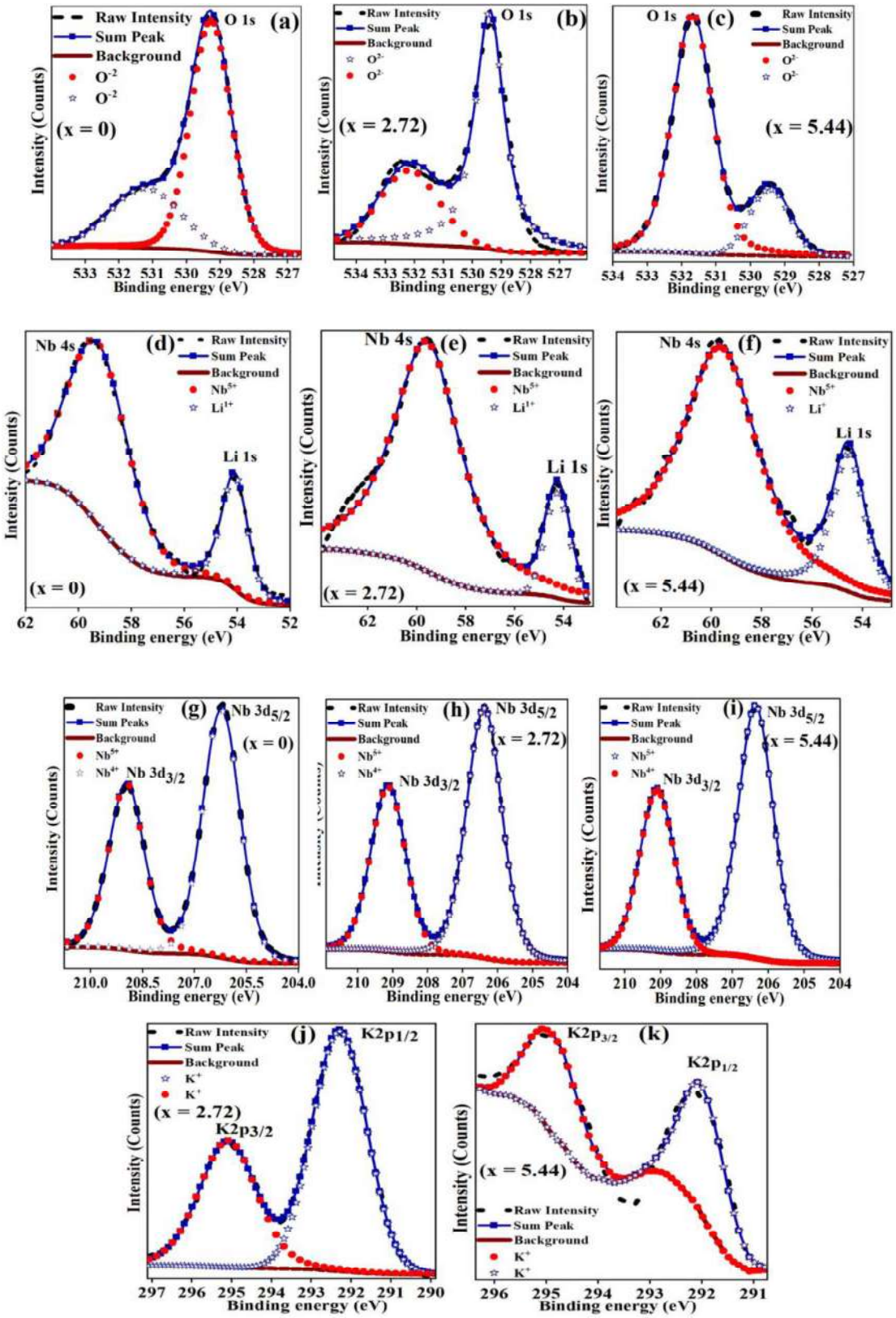

Figure 3.9:(a-k) X-ray photo electron spectra of various elements for pure LN, and LN with 2.72 wt% and 5.44 wt % K_2O additive concentration.

peaks are observed at binding energies of 295.11 eV, 292.28 eV for 2.72 wt% K_2O and 295.10 eV, 292.07 eV for 5.44 wt% K_2O additive concentrations. The position of the two peaks at these binding energies are almost similar to that reported in previous literature[17,21].

3.4.4 Fourier Transform Infrared spectroscopy

FTIR characterization has been performed to confirm the quality and consistency of the samples and the spectra for pure LN, and LN with 2.72 wt% and 5.44 wt% K_2O additive concentration are shown in the **Figure 3.10.** A broad and strong peak at 3445 cm^{-1} is attribute to stretching vibration of O-H bond[23]. A very weak peak at 2980 cm^{-1} also attribute to stretching vibration of O-H bond but it disappears for 5.44 wt% addition of K_2O. At 1635 cm^{-1} a weak peak appear which is attributed to OH vibrations due to moisture in atmosphere[24]. A strong and intense peak observed at 1140 cm^{-1} belongs to the stretching vibration of C-O bond. The peak at 620 cm^{-1} and 660 cm^{-1} are assigned to Li-O and Nb-O bond and vibration which is characteristic of crystalline perovskite phase of the samples[25,26]. The IR absorption of $LiNbO_3$ also occurs in the range of 600–700 cm^{-1}[27]. The formation of nano crystallinity is confirmed by the appearance of peak at around 425 cm^{-1}.

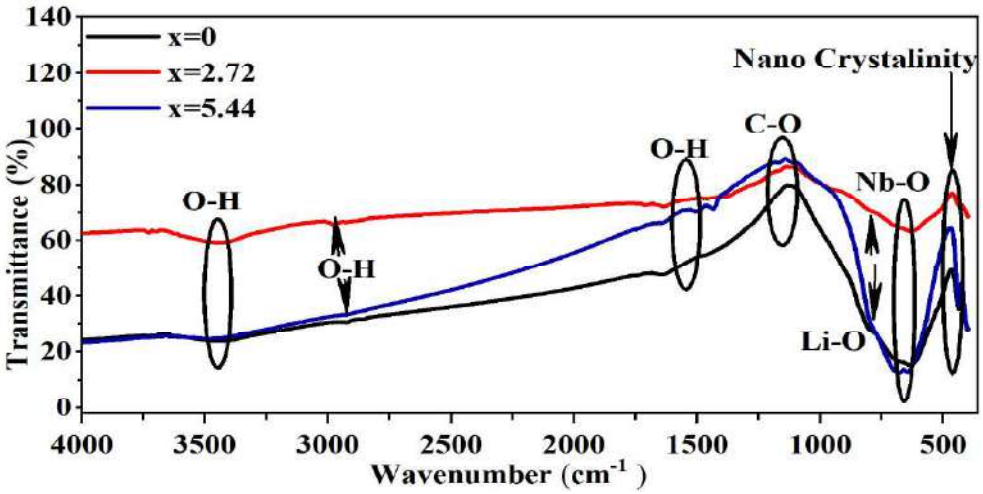

Figure 3.10: FTIR Spectra for the pure LN, and LN with 2.72 wt% and 5.44 wt % K_2O additive concentration.

3.4.5 Thermogravimetric analysis

TGA characterization of the samples has been performed in the temperature range 21°C to 900°C to get the idea about weight loss at higher temperatures for applications under non-ambient conditions. As shown in the **Figure 3.11(a)**, it is observed that pure lithium niobate as well as K_2O added lithium niobate show weight loss at higher temperatures and exhibit partial decomposition in one or more steps. It is calculated that the overall weight loss of pure LN, 2.72 wt% and 5.44 wt% K_2O added LN are 2.15%, 3.09% and 3.31% respectively. Kinetic parameters such as energy of activation for all the samples have been evaluated using Broido process[28]. 51 It has been known that Broido process uses following equations for the evaluation of energy of activation for all decomposition stages w.r.t. temperature.

$$\ln\left(\ln\left(\frac{1}{y}\right)\right) = \frac{E_a}{RT} + \text{Constt} \qquad \ldots\ldots\ldots\ldots\ldots\ldots\ldots\ldots 3.1$$

$$Y = \frac{(Wt - W\infty)}{(Wo - W\infty)} \qquad \ldots\ldots\ldots\ldots\ldots\ldots\ldots\ldots 3.2$$

Activation Energy (E_a) = –2.303 ×R ×slope

Where R stands for the gas constant, Wt = weight of sample at absolute temperature T,
W∞ = weight of the sample at the end of the temperature of the thermogram,
Wo = weight of the sample at the start of the temperature of the thermogram.

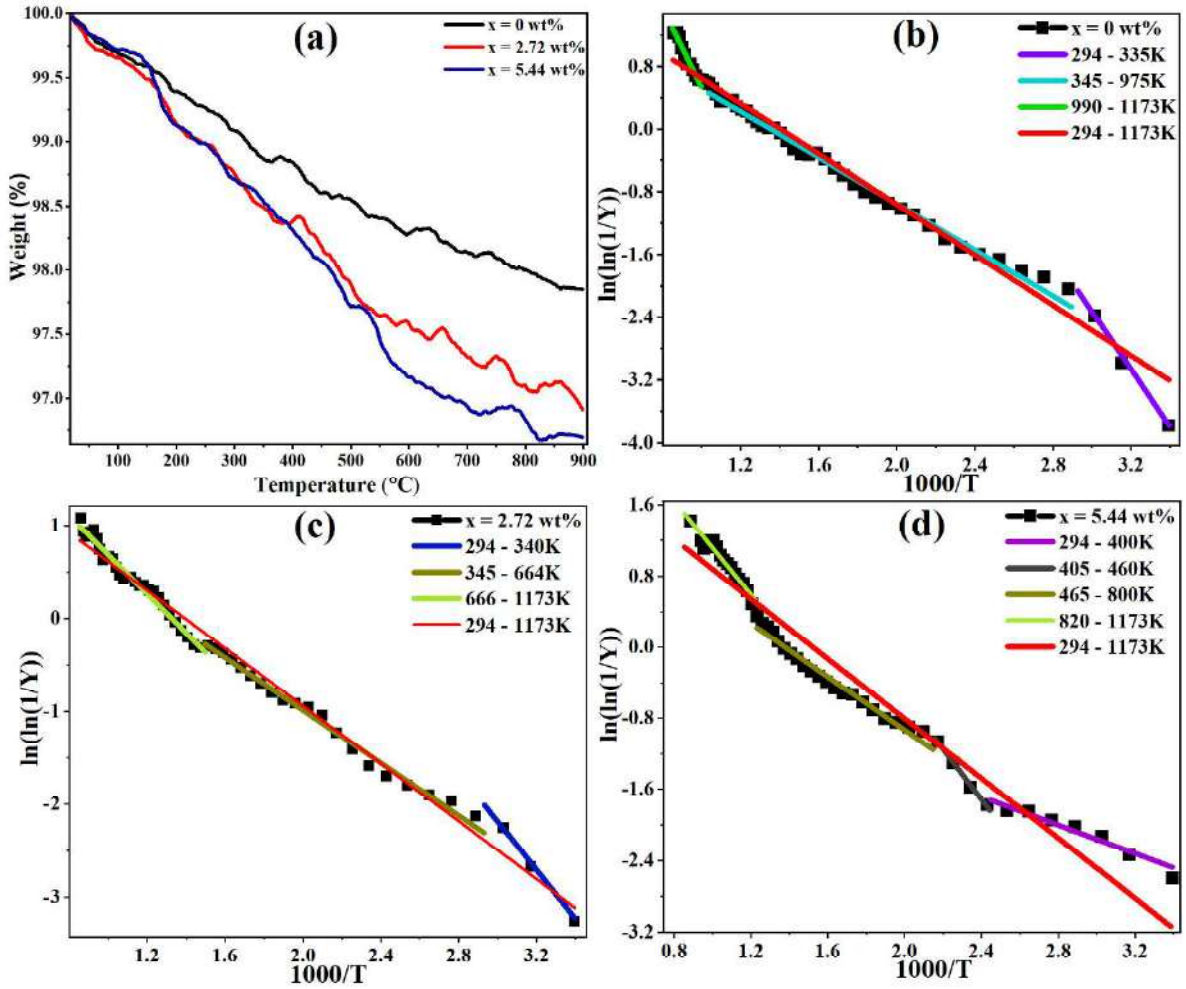

Figure 3.11(a-d): (a) Thermograph of pure LN, and LN with 2.72 wt% and 5.44 wt% K_2O additive, (b) Plot of ln(ln(1/Y)) vs 1000/T for, pure LN, (c) x = 2.72 wt% K_2O, (d) x = 5.44 wt% K_2O.

Using equation 1 and 2 [29], and taking the slope of the straight line between ln(ln(1/Y)) and 1000/T for different temperature stages, it is clearly observed that the pure LN and with 2.72% K_2O have 3 temperature stages whereas LN with 5.44% K_2O has 4 temperature stages having 4 different energies of activation. Energy of activation for full temperature range is evaluated for all the samples and a comparison is plotted in the **Figure 3.12(a-c)**. We found that 2.72% K_2O added LN has higher energy of activation among all the samples and hence more stable than the other composition. This composition has energy of activation high among all the samples even in different temperature ranges which signify its

high stability in throughout temperature region. The LN with 5.44% K_2O additive also has higher energy of activation as compared to pure LN in different temperature stages. In selected temperature ranges, pure LN has higher value of E_a for (350-980K); LN with 2.72% K_2O for (345-664K) and LN with 5.44% K_2O for (294-400K), respectively.

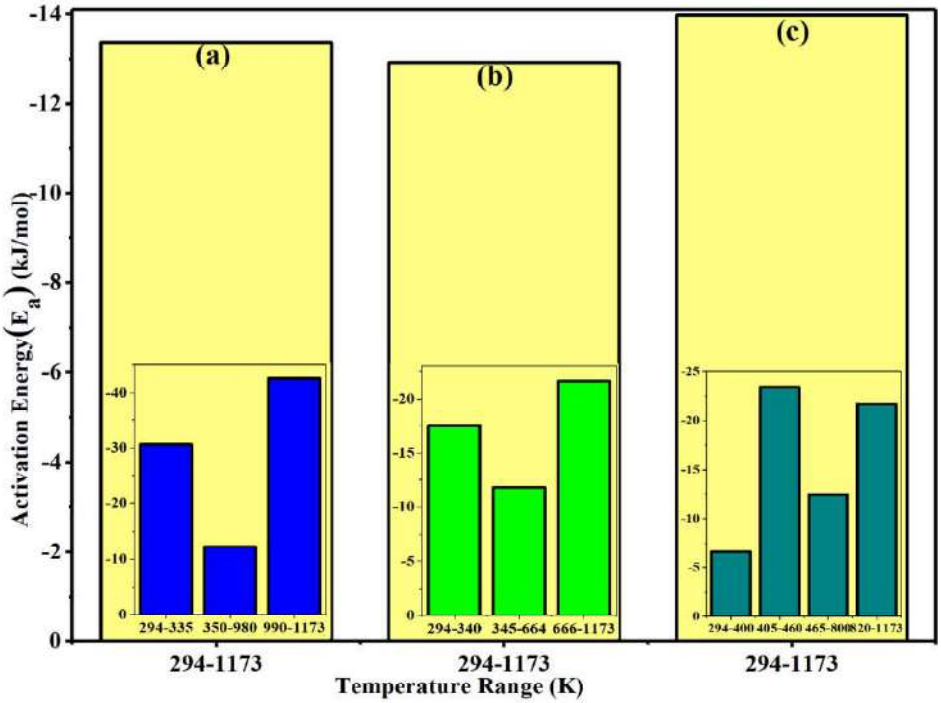

Figure 3.12(a-c): Histogram of activation energy in different temperature range for (a) $LiNbO_3$ (b) LN with 2.72 wt% K_2O, (c) LN with 5.44 wt% K_2O.

3.4.6 Optical Properties and band gap analysis

The effect of potassium oxide (K_2O) additive on the optical properties of LN for various concentrations is investigated and the optical absorption spectra is illustrated in the **Figure 3.13(a).** Using the well-known Tauc equation, $\alpha h\nu = B(h\nu - E_g)^{1/2}$, where $h\nu$ is the band gap energy, α is absorption coefficient, and B is referred to as the Tauc constant[30], the indirect band gap for various compositions is determined from $(\alpha h\nu)^{0.5}$ versus $h\nu$ plot. As shown in the **Figure 3.13 (b)**, pure $LiNbO_3$ exhibits a substantially lower indirect band gap value (E_g = 2.33

eV) than the value that is previously published in the literature (E_g = 3.3 eV)[31]. With increasing the K_2O additive concentration in $LiNbO_3$, the indirect band gap decreases but there is no clear tangent line observed and so we have calculated the direct band gap. The direct band gap of LN with K_2O additive were determined using the Tauc's equation $\alpha h\nu = B(h\nu - E_g)^2$[30]. The direct band gap values are obtained by drawing a tangent line on $(\alpha h\nu)^2$ vs $h\nu$ plot as shown in **Figure 3.13 (c)** [32]. With the K_2O addition in $LiNbO_3$, the direct band gap decreases to 3.04 eV for 1.36 wt% addition and further decreased to 2.36 eV for 2.72 wt% K_2O addition. When additive percentage further increased (4.08 wt%), it is observed that band gap values start increasing as shown in the **Figure 3.13 (d)**. This increase in band gap for 4.08 wt% K_2O addition and 5.44 wt% K_2O addition in LN, can be related to new phases formed as indicated in XRD patterns.

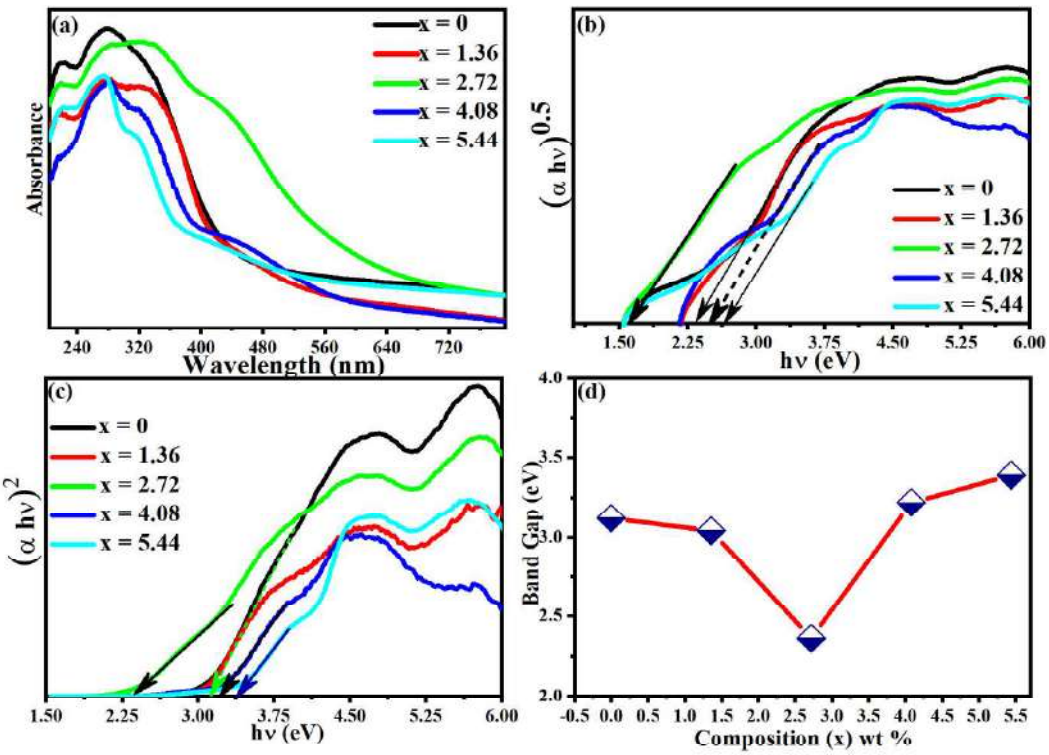

Figure 3.13 (a-d): (a) Absorption spectra; (b) Indirect band gap; (c) Direct band gap of LN with various concentration of K_2O additive in the range ($0.0 \leq x$ (wt%) ≤ 5.44). (d) Variation of direct band gaps as a function of K_2O additive concentration.

The greater absorption in the visible range for the composition with 2.72 wt% K_2O additive is obtained, which may be caused by coupling between K ions and oxygen vacancies[33]. Due to K_2O addition and the presence of oxygen vacancies, this composition also has the lowest band gap (2.36 eV). Vacancies form the sub-bands between the conduction band minimum (CBM) and valence band maximum (VBM) and thus CBM tail is prolonged and the band gap is decreased[34]. Valence bands of K-doped $LiNbO_3$ mainly consisted of O 2p states while their conduction bands mainly consist of Nb-4d states. In case of Li and Nb vacancies, an acceptor level in the band gap may be created at the top of the valence band and in case of oxygen vacancies, a donor level under the bottom of the conduction band may be created[35]. So, we may consider that there is shifting of both CBM and VBM leading to band gap reduction. The decrease in band gap can be due to vacancies which cause downward shifting of the CBM and also due to upward shifting of VBM. Our explanation is also supported by previous studied on band gap of perovskite oxides[36–38]**.**

3.4.7 Photoluminescence properties

We examined the composition-dependent photoluminescence (PL) emission for LN with various K_2O additive concentration at ambient temperature. The PL emission characterization of LN and K_2O added LN is conducted between 500 and 600 nm. The samples were excited at 465 nm wavelength. As shown in the **Figure 3.14**, pure LN and K_2O added LN compositions exhibit PL emission in the UV-visible light region and exhibit an intense peak of green colour emission at 517-547 nm. This intense emission peak of green colour luminescence was detected in all samples. Potassium Oxide added LN compositions also showed two weak PL emission peaks in the UV-visible spectral region around 558-592 nm and 694-708 nm, as shown in the **Figure 3.14**. The second broad peak in the range 558-592

nm is attributed to yellow colour spectrum. Third weak band in the range 694-708 nm is related to red colour spectrum. So, all the compositions of LN with K_2O additive show green, yellow and red emission peaks. The green peak at 526 nm produced in all compositions of LN with K_2O are due to potassium oxide addition and defect energy levels developed which cause such emissions. When $LiNbO_3$ is added with K_2O, oxygen vacancies are produced. These oxygen vacancies create new energy levels to form sub-bands. Green emission results from fully ionized oxygen vacancies[39,40]. Dislocations, surface defects, oxygen vacancies, or point defects may be the cause of the yellow and red band in PL spectra[41]. The donor-acceptor pair recombination zone found inside depletion regions connected to grain interfaces is where the yellow emission band originates. Donor-acceptor pair type transition is the

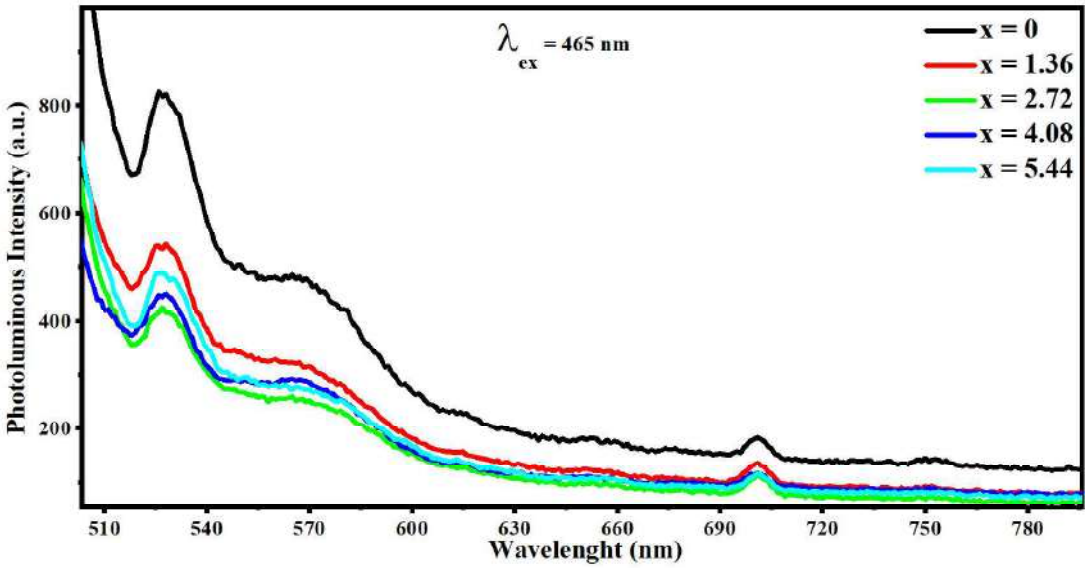

Figure 3.14: Photoluminescence spectra for LN with different concentration of K_2O additive.

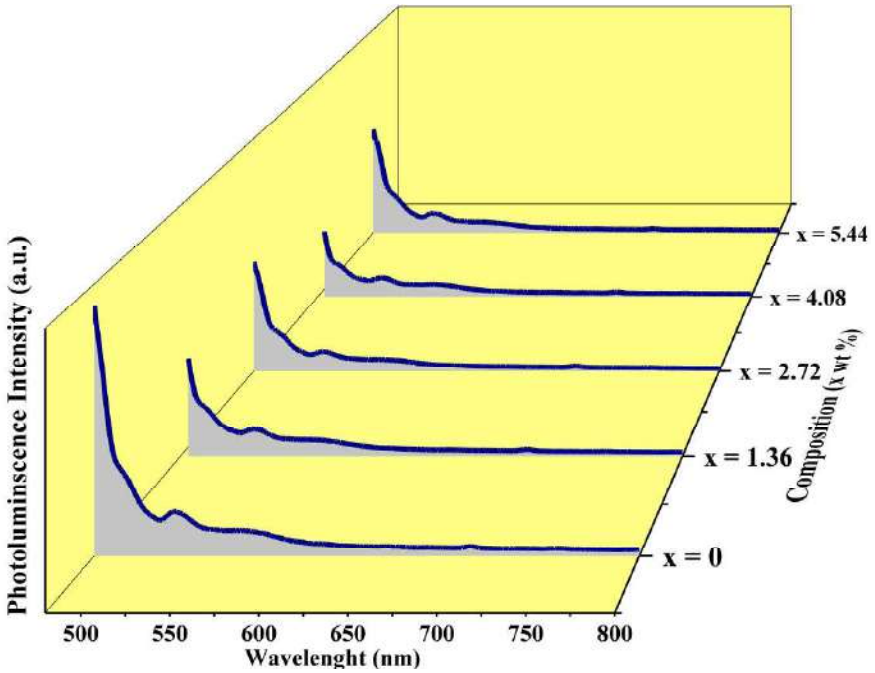

Figure 3.15: Photoluminescence spectra for LN with different concentration of K_2O additive in 3D form.

cause of this yellow band transformation[41]. Luminescence intensity starts to decrease with increasing the amount of potassium oxide addition in $LiNbO_3$ because of the lattice distortion, presence of vacancies and decreased charge recombination rate. With further K_2O (4.08 wt%) addition, emission intensity slightly increased which can be related to a decrease in grain boundaries and increased surface oxygen vacancies.

3.4.8 Dielectrics analysis

The **Figure 16 (a-f),** shows dielectric characterizations at high temperature of LN pellets with different additive concentration of K_2O. The measurement is performed on pellets sintered at 1050°C for 6 hours and then applying silver electrodes. The dielectric constant (ε') is calculated using the relation $\varepsilon' = Cd/\varepsilon_0 A$ and the ac conductivity is calculated by the relation, $\sigma_{ac} = \varepsilon_0 \varepsilon_r \omega \tan(\delta)$, where C is the measured pellet capacitance, d is the thickness, A is the area

of cross section of the pellet and tan(δ) is the dielectric relaxation loss of the sample. The temperature dependence of dielectric constant and dielectric loss is shown in the **Figure 3.16 (a-f)** at different frequencies. The value of $\varepsilon^{/}$ increases with temperature but decreases with frequency for all measured temperature range. This happen because the contributions of electronic and ionic polarization are less at lower temperatures but start to increase significantly with rise of temperature. The dielectric constant values increase slowly with temperature rise but became rapid after 350°C. This rapid increase of dielectric constant happens because lithium ion start hopping between the thermally activated oxygen vacancies. While for the low frequencies electronic, ionic, dipolar and interfacial components are put up for the total polarization so that $\varepsilon^{/}$ is high but when frequencies increase the interfacial and dipolar polarizations lag behind the ac-electric field resulting lesser value of $\varepsilon^{/}$ at higher frequencies. The dielectric constant of $LiNbO_3$ increases with K_2O addition due to the increased concentration of mobile ions in the crystal. Some potassium ions substitute for lithium ions in the crystal lattice, creating a higher concentration of mobile Li-ions that can respond to an applied electric field, leading to a higher dielectric constant. Additionally, addition of K_2O can also lead to the formation of defects in the crystal lattice, which can also contribute to the increased dielectric constant. The K_2O added $LiNbO_3$ crystals can contain polar clusters formed by impurities and native defects localized along the polar axis. These defects, which are created by the substitution of impurities for native ions in the crystal lattice, can have a significant impact on the electrical conductivity and dielectric properties of the material.

The presence of polar clusters in K_2O added $LiNbO_3$ crystals can also affect the electrical conductivity of the material by creating a higher concentration of mobile Li-ions

that can respond to an applied electric field, resulting in an increase in conductivity. On the other hand, polar clusters can also affect the dielectric properties of the material by creating defects in the crystal lattice that can negatively impact the ability of the material to store electrical energy in an electric field, resulting in a decrease in dielectric constant[42–44]. Further, it is understood that the activation energy plays a pivotal role in determining the polarization mechanisms within a material. High activation energy levels can limit the movement of charge carriers, thereby affecting parameters such as dielectric constant ($\varepsilon^{/}$), and loss tangent (tanδ). One has to be careful while explaining this phenomena, as the impact of polar clusters on the electrical conductivity and dielectric properties of K_2O added $LiNbO_3$ crystals can vary depending on the specific impurities and defects present, as well as the concentration of these impurities. So, higher amount of additive can lead to decrement in the dielectric constant[45–50].

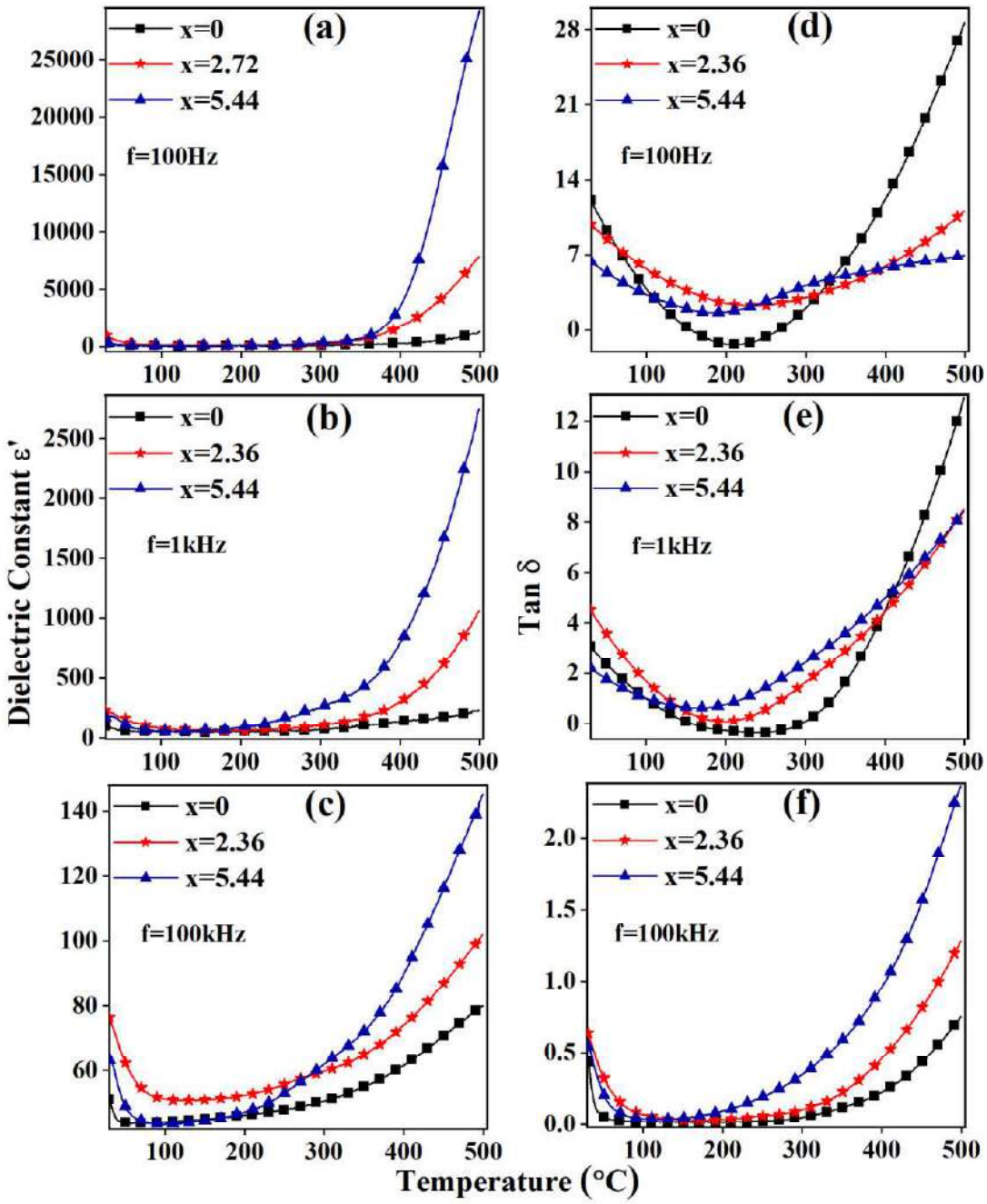

Figure 3.16(a-f); Temperature and frequency (l00Hz to 100kHz) dependent dielectric behaviour of LN with different K_2O additive concentration.

3.4.9 Polarization electric field analysis

The P-E hysteresis loops of pure LN and with different concentration of K_2O additive were measured at room temperature using ac- triangular waveform at different frequencies.

The samples were kept in temperature-controlled chamber in the presence of silicon oil [13]. The P-E hysteresis loop of poled samples of LN and K_2O added LN are shown in the **Figure 3.17(a-e)** with the measuring frequencies mentioned in the respective plots. the **Figure 3.17(a)** shows P-E loop for the pure LN ceramic sample in the frequency range from 150 Hz to 300 Hz. It is observed that at applied field of 70kV/cm and applied frequency of 200 Hz, the maximum polarization value is 0.69 $\mu C/cm^2$. For all the compositions, when the measuring frequency is increased, the P-E loop become slightly narrow due to vanishing contribution of defect induced polarization. The frequency dependence of P-E loops is more pronounced for higher K_2O additive concentration as the higher defect centers are expected in these compositions. The P-E loop for 1.36 wt% K_2O addition is depicted in the **Figure 3.17(b)** showing maximum polarization of 0.99 $\mu C/cm^2$. For the 2.72 wt % K_2O addition, the P-E hysteresis loop is more lossy in nature but the polarization is increased up to 1.16 $\mu C/cm^2$, as shown in the **Figure 3.17(c).** As discussed earlier, the grain size reduces up to 2.72 wt % K_2O addition. The more number of grain boundary interfaces also may act as charge trappers which can lead to the increased ferroelectric loss. With further increasing K_2O additive concentration to 4.08, it can have observed that the P-E hysteresis loop become narrower with a maximum polarization value of 0.71 $\mu C/cm^2$, as shown in the **Figure 3.17(d)**. The highest polarization value of 0.44 $\mu C/cm^2$ is obtained for the 5.44 K_2O additive concentration with very slim P-E loop as shown in the **Figure 3.17(e).** As confirmed from SEM micrographs, the average grain size start increasing beyond a certain amount of K_2O additive in the LN ceramic. The larger grain size can inhibit the domain wall motion by reducing the ability of domains to switch which results into reduced overall polarization of this composition. The large grain size may also lead to lower grain boundary interfaces defects with less charge trappers in the system so

that the P-E loop is not lossy in nature for 5.44 wt% K_2O additive concentration. Banerjee et al. have reported polarization-electric field hysteresis measurements on mesoporous lithium niobate samples with polarization value of 0.00026 μC/cm^2 which is very low as compared to our results[51]. In an earlier study on $La_{0.05}Li_{0.85}NbO_3$ ceramics, the polarization values of Ps = 0.235 μC/cm^2 and Pr = 0.141 μC/cm^2 are reported [52]. Our present work demonstrates substantially improved polarization in comparison to those reported in existing literature. Addition of potassium oxide results in the formation of more oxygen vacancies in the crystal lattice. The oxygen vacancies create an imbalance of charges leading to permanent alignment of the electric dipoles resulting in a higher remnant polarization [53–55]. The Excess addition of K_2O leads to decrement in the polarization because of the deficiency of Li ions in K_2O added LN due to partial substitution of Li^+ by K^+ and associated defect formation [56].

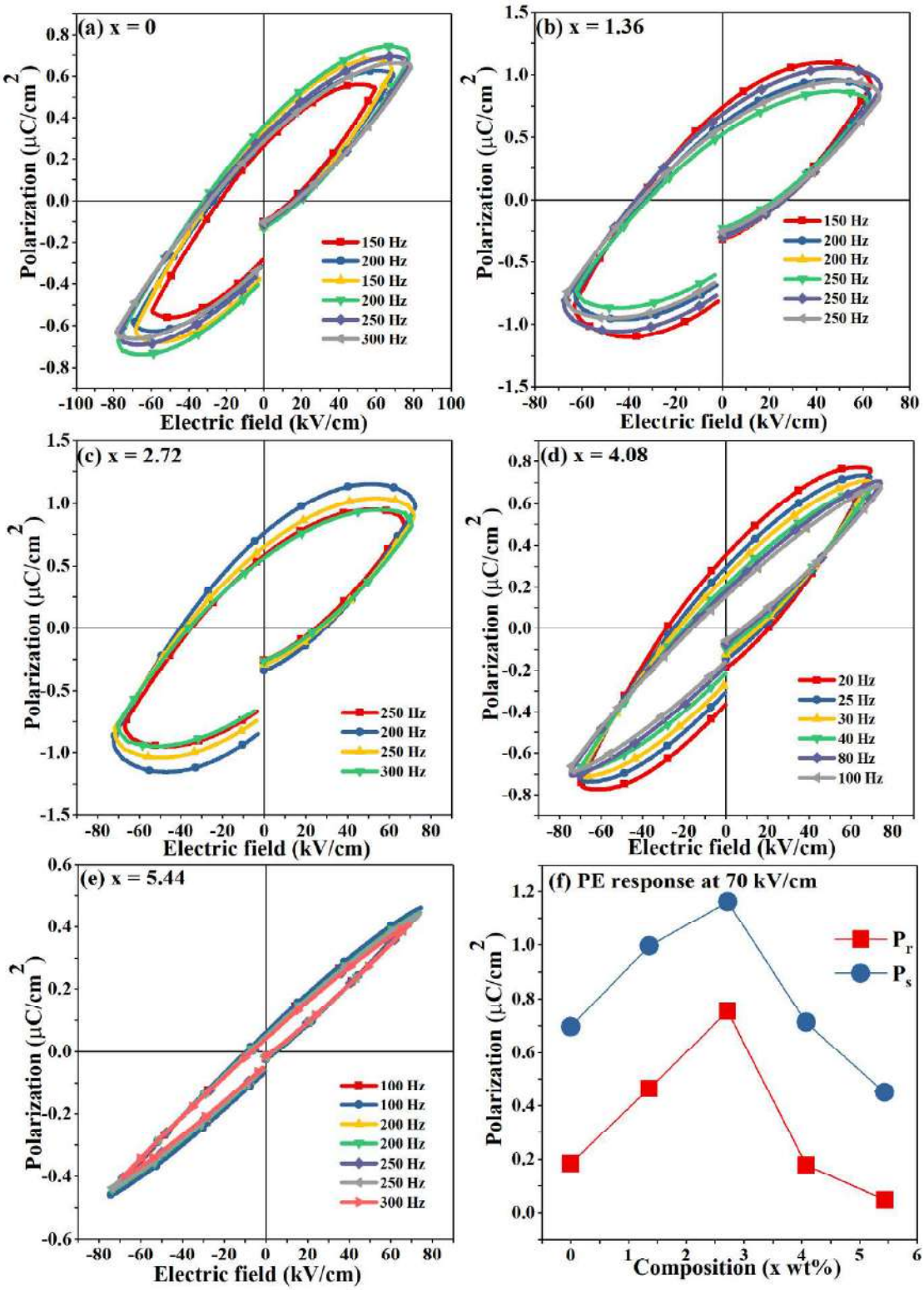

Figure 3.17(a-f): (a-e) Polarization-Electric field ferroelectric hysteresis loops for LN with different concentrations of K_2O additive, (f) Composition dependence of polarization at 70 kV/cm field.

3.5 Conclusions:

Dense $LiNbO_3$ crystalline ferroelectric ceramics have been successfully synthesized by using K_2O additive of different concentrations. The Le bail structural refinement of XRD patterns confirm that the crystal structure of $LiNbO_3$ is rhombohedral with R3c space group for pure as well as K_2O added concentrations upto 5.44 wt.%. Higher K_2O additive concentration beyond 2.44 wt.% leads to appearance of secondary cubic phase of K_2O. The average grain size of $LiNbO_3$ decreases initially with K_2O addition but start increasing for higher additive concentration. Thermal analysis of the samples reveals that use of K_2O is increasing the thermal stability of the LN with improved properties and best thermal stability is obtained for 2.72 wt.% K_2O additive concentration. The XPS measurements reveal that position of satellite peaks of O 1s shifts as the concentration of K_2O additive increases since the hygroscopic nature of potassium increases the absorbed moisture in the system. The optical band gap of LN decreases from 3.12eV to 2.36 eV up to 4.08 additive concentration and thereafter slightly increases for higher K_2O addition. Decrease in band gap can be related to presence of defects induced sub-bands between CBM and VBM. Photoluminescence study confirms intense emission in green color spectrum followed by yellow and red color emission spectra. Visibility of green color spectra in all compositions also confirms presence of oxygen vacancies. The room temperature dielectric permittivity of LN at 1kHz frequency is found to increase from 97.29 to 233.15 by using 2.72 wt.% K_2O additive while the remnant polarization is increased from 0.18$\mu C/cm^2$ to 0.75 $\mu C/cm^2$. The developed material can be very useful for advanced technological applications at non-ambient temperatures.

References:

[1] D. Sugak, L. Vasylechko, V. Sydorchuk, S. Hurskyy, A. Luchechko, I.I. Syvorotka, A. Lakhnik, U. Yakhnevych, V. Hreb, S. Ubizskii, Y. Suhak, Mechanosynthesis, Structure and Photoluminescent Properties of the Pr^{3+} Doped $LiNbO_3$, $LiNbO_3$:Mg, $LiTaO_3$ Nanopowders, Powders. 2 (2023) 562–577. https://doi.org/10.3390/powders2030035.

[2] Y. Batra, Manipulation of domain structures in $LiNbO_3$ thin films using focused ion beam, Phys. B Condens. Matter. 677 (2024) 415693. https://doi.org/10.1016/j.physb.2024.415693.

[3] M.A. Fakhri, U. Hashim, E.T. Salim, Z.T. Salim, Preparation and charactrization of photonic $LiNbO_3$ generated from mixing of new raw materials using spry pyrolysis method, J. Mater. Sci. Mater. Electron. 27 (2016) 13105–13112. https://doi.org/10.1007/s10854-016-5455-8.

[4] X. Zeng, X. Zhang, V. Pelenovich, D. Neena, C. Xu, Y. Liu, Y. Jiang, L. Zeng, A. Pogrebnjak, R. Vildanov, A. Ieshkin, R. Rakhimov, J. Zhang, B. Yang, S. Liu, High-temperature thin film lithium niobium oxide transducers for bolts, Ceram. Int. 49 (2023) 7710–7716. https://doi.org/10.1016/j.ceramint.2022.10.262.

[5] S.K. Satyarthi, The Study of MgO Nano-Composite : Synthesis , Characterization and Probable Application Submitted in partial fulfillment of the requirement.

[6] R. Bhatt, S. Kar, K.S. Bartwal, V.K. Wadhawan, The effect of Cr doping on optical and photoluminescence properties of $LiNbO_3$ crystals, Solid State Commun. 127 (2003) 457–462. https://doi.org/10.1016/S0038-1098(03)00450-2.

[7] R. Priya, S. Kainth, D. Kumar, P. Sharma, P.K. Diwan, O.P. Pandey, Investigating transformation kinetics of yttrium hydroxide to yttrium oxide, Mater. Chem. Phys. 287 (2022) 126243. https://doi.org/10.1016/j.matchemphys.2022.126243.

[8] A. Le Bail, H. Duroy, J.L. Fourquet, Ab-initio structure determination of LiSbWO6 by X-ray powder diffraction, Mater. Res. Bull. 23 (1988) 447–452. https://doi.org/10.1016/0025-5408(88)90019-0.

[9] V.K. Peterson, Lattice parameter measurement using Le Bail versus structural (Rietveld) refinement: A caution for complex, low symmetry systems, Powder Diffr. 20 (2005) 14–17. https://doi.org/10.1154/1.1810156.

[10] A.E. Sanches, M.S. Souza, L.P.A. Carvalho, G. Trovati, E.G.R. Fernandes, Y.P. Mascarenhas, The use of Le Bail Method to Analyze the semicrystalline Pattern of a Nanocomposite based on Polyaniline Emeraldine-Salt form base and α -Al_2O_3, Int. J. Mater. Res. 106 (2015).

[11] V.P. Singh, C.B. Singh, S.K. Satyarthi, D. Kumar, A.K. Singh, Highly enhanced energy storage properties of H_2O_2-hydroxylated rare earth ferrites ($LaFeO_3$ and $GdFeO_3$) nanofillers in poly(vinylidene fluoride)-based nanocomposite films, J. Mater. Sci. Mater. Electron. 33 (2022) 20170–20184. https://doi.org/10.1007/s10854-022-08836-z.

[12] V.P. Singh, S.K. Satyarthi, A. Dwivedi, A. Dwivedi, A.K. Singh, Boosting Energy Storage of Poly(vinylidene difluoride) Nanocomposite Based Flexible Self-Standing Film with Low Amount of Hydroxylated V_2O_5, ACS Appl. Energy Mater. 5 (2022) 12837–12850. https://doi.org/10.1021/acsaem.2c02425.

[13] V.P. Singh, S.K. Satyarthi, S. Paliwal, A.K. Singh, Enhancement in Polarization and Energy Density of PVDF Matrix Using Hydroxylated CeO_2-NPs as Filler in Nanocomposite Thick Film, IEEE Int. Symp. Appl. Ferroelectr. ISAF 2023, Int. Symp. Integr. Funct. ISIF 2023 Piezoresponse Force Microsc. Work. PFM 2023, Proc. (2023) 1–4. https://doi.org/10.1109/ISAF53668.2023.10265521.

[14] A. Dwivedi, V.P. Singh, A. Dwivedi, A.K. Singh, Synthesis and electrical characterization of cold sintered $Ba_{0.7}Sr_{0.3}TiO_3$–PVDF ceramic nanocomposites for capacitive energy storage applications, J. Mater. Sci. Mater. Electron. 34 (2023) 1–15. https://doi.org/10.1007/s10854-023-11358-x.

[15] W. Xie, R. Li, Q. Xu, Enhanced photocatalytic activity of Se-doped TiO_2 under visible light irradiation, Sci. Rep. 8 (2018) 1–10. https://doi.org/10.1038/s41598-018-27135-4.

[16] W. Cui, H. Wang, Y. Liang, B. Han, L. Liu, J. Hu, Microwave-assisted synthesis of Ag@AgBr-intercalated $K_4Nb_6O_{17}$ composite and enhanced photocatalytic degradation of Rhodamine B under visible light, Chem. Eng. J. 230 (2013) 10–18. https://doi.org/10.1016/j.cej.2013.03.091.

[17] S. Das, D. Dutta, R.B. Araujo, S. Chakraborty, R. Ahuja, A.J. Bhattacharyya, Probing the pseudo-1-D ion diffusion in lithium titanium niobate anode for Li-ion battery, Phys. Chem. Chem. Phys. 18 (2016) 22323–22330. https://doi.org/10.1039/c6cp04488c.

[18] P. Steiner, H. Höchst, X-ray excited photoelectron spectra of $LiNbO_3$: A quantitative analysis, Zeitschrift Für Phys. B Condens. Matter Quanta. 35 (1979) 51–59. https://doi.org/10.1007/BF01322081.

[19] M.M.S. Sanad, A. Toghan, Chemical activation of nanocrystalline $LiNbO_3$ anode for improved storage capacity in lithium-ion batteries, Surfaces and Interfaces. 27 (2021) 101550. https://doi.org/10.1016/j.surfin.2021.101550.

[20] J. Piecha, A. Molak, U. Breuer, M. Balski, K. Szot, Features of surface layer of $LiNbO_3$ as-received single crystals: Studied in situ on treatment samples modified by elevated temperature, Solid State Ionics. 290 (2016) 31–39. https://doi.org/10.1016/j.ssi.2016.04.001.

[21] L. Yan, G. Chen, S. Sarker, S. Richins, H. Wang, W. Xu, X. Rui, H. Luo, Ultrafine Nb_2O_5 Nanocrystal Coating on Reduced Graphene Oxide as Anode Material for High Performance Sodium Ion Battery, ACS Appl. Mater. Interfaces. 8 (2016) 22213–22219. https://doi.org/10.1021/acsami.6b06516.

[22] M. Aufray, S. Menuel, Y. Fort, J. Eschbach, D. Rouxel, B. Vincent, New synthesis of nanosized niobium oxides and lithium niobate particles and their characterization by XPS analysis, J. Nanosci. Nanotechnol. 9 (2009) 4780–4785. https://doi.org/10.1166/jnn.2009.1087.

[23] R.K. Choubey, B.Q. Khattak, S. Kar, P. Ramshankar, P. Sen, K.S. Bartwal, Influence of doping on OH absorption in $LiNbO_3$ crystals, Cryst. Res. Technol. 42 (2007) 718–722. https://doi.org/10.1002/crat.200610894.

[24] L. Kovács, M. Wohlecke, A. Jovanović, K. Polgár, S. Kapphan, Infrared absorption study of the OH vibrational band in $LiNbO_3$ crystals, J. Phys. Chem. Solids. 52 (1991) 797–803. https://doi.org/10.1016/0022-3697(91)90078-E.

[25] G. Bhagavannarayana, R. V. Ananthamurthy, G.C. Budakoti, B. Kumar, K.S. Bartwal, A study of the effect of annealing on Fe-doped $LiNbO_3$ by HRXRD, XRT and FT–IR, J. Appl. Crystallogr. 38 (2005) 768–771. https://doi.org/10.1107/S0021889805023745.

[26] C. An, K. Tang, C. Wang, G. Shen, Y. Jin, Y. Qian, Characterization of $LiNbO_3$ nanocrystals prepared via a convenient hydrothermal route, Mater. Res. Bull. 37 (2002) 1791–1796. https://doi.org/10.1016/S0025-5408(02)00869-3.

[27] P.M. Vilarinho, N. Barroca, S. Zlotnik, P. Félix, M.H. Fernandes, Are lithium niobate ($LiNbO_3$) and lithium tantalate ($LiTaO_3$) ferroelectrics bioactive?, Mater. Sci. Eng. C. 39 (2014) 395–402. https://doi.org/10.1016/j.msec.2014.03.026.

[28] K. R. Patel, Dhara Patel,V D Patel, characterization, activation energy and thermodynamic parameter of crystals synthesized from solvent evaporation method, Int. J. Res. Biosci. Agric. Technol. (2014) 746–753. https://doi.org/10.29369/ijrbat.2014.02.II.0070.

[29] J.M. Rami, C.D. Patel, C.M. Patel, M. V. Patel, Thermogravimetric analysis (TGA) of some synthesized metal oxide nanoparticles, Mater. Today Proc. 43 (2020) 655–659. https://doi.org/10.1016/j.matpr.2020.12.554.

[30] J. Tauc, Optical properties and electronic structure of amorphous Ge and Si, Mater. Res. Bull. 3 (1968) 37–46. https://doi.org/10.1016/0025-5408(68)90023-8.

[31] S. Çabuk, A. Mamedov, Urbach rule and optical properties of the $LiNbO_3$ and $LiTaO_3$, J. Opt. A Pure Appl. Opt. 1 (1999) 424–427. https://doi.org/10.1088/1464-4258/1/3/313.

[32] C.B. Singh, D. Kumar, N.K. Verma, A.K. Singh, Structural, dielectric, semiconducting and optical properties of high-energy ball milled $YFeO_3$ nano-particles, AIP Conf. Proc. 2115 (2019) 8–12. https://doi.org/10.1063/1.5113458.

[33] L. Mühlenbein, C.B. Singh, A.K. Singh, I. Fina, C. Himcinschi, A. Lotnyk, A. Bhatnagar, Control of Layering in Aurivillius Phase Nanocomposite Thin Films and Influence on Ferromagnetism and Optical Absorption, ACS Appl. Electron. Mater. 4 (2022) 1997–2004. https://doi.org/10.1021/acsaelm.2c00160.

[34] C. Bhal Singh, N. Kumar Verma, A. Kumar Singh, Synthesis and band-gap tuning of (Co, Bi) doped $PbTiO_3$ for photoferroelectrics applications, Integr. Ferroelectr. 194 (2018) 145–151. https://doi.org/10.1080/10584587.2018.1514886.

[35] A. Shigemi, T. Wada, Evaluations of phases and vacancy formation energies in $KNbO_3$ by first-principles calculation, Japanese J. Appl. Physics, Part 1 Regul. Pap. Short Notes Rev. Pap. 44 (2005) 8048–8054. https://doi.org/10.1143/JJAP.44.8048.

[36] D. Mala, C.B. Singh, A.K. Singh, Band gap Engineering of $BaTi_{1-x}$ $(Ni_{1/3}Nb_{2/3})xO_3$ Ceramics for Ferro-Photovoltaic Applications, IEEE Int. Symp. Appl. Ferroelectr. ISAF 2023, Int. Symp. Integr. Funct. ISIF 2023 Piezoresponse Force Microsc. Work. PFM 2023, Proc. (2023) 1–4. https://doi.org/10.1109/ISAF53668.2023.10265387.

[37] P.J. Niu, J.L. Yan, C.Y. Xu, First-principles study of nitrogen doping and oxygen vacancy in cubic $PbTiO_3$, Comput. Mater. Sci. 98 (2015) 10–14. https://doi.org/10.1016/j.commatsci.2014.10.057.

[38] D. Kumar, S. Yadav, C.B. Singh, R.S. Yadav, S.B. Rai, A.K. Singh, Impact of Sr^{2+} doping on the structural, dielectric, ferroelectric and optical properties of $YFeO_3$ perovskite phosphor, J. Alloys Compd. 945 (2023) 169286. https://doi.org/10.1016/j.jallcom.2023.169286.

[39] C.L. Kuo, Y.S. Chang, Y.H. Chang, W.S. Hwang, Synthesis of nanocrystalline lithium niobate powders via a fast chemical route, Ceram. Int. 37 (2011) 951–955. https://doi.org/10.1016/j.ceramint.2010.11.008.

[40] G. Dominiak-Dzik, W. Ryba-Romanowski, M.N. Palatnikov, N. V. Sidorov, V.T. Kalinnikov, Dysprosium-doped $LiNbO_3$ crystal. Optical properties and effect of temperature on fluorescence dynamics, J. Mol. Struct. 704 (2004) 139–144. https://doi.org/10.1016/j.molstruc.2004.01.063.

[41] M. Matys, B. Adamowicz, Mechanism of yellow luminescence in GaN at room temperature, J. Appl. Phys. 121 (2017). https://doi.org/10.1063/1.4975116.

[42] R. Gao, Q. Zhang, Z. Xu, Z. Wang, G. Chen, X. Deng, C. Fu, W. Cai, A comparative study on the structural, dielectric and multiferroic properties of $Co_{0.6}Cu_{0.3}Zn_{0.1}Fe_2O_4/Ba_{0.9}Sr_{0.1}Zr_{0.1}Ti_{0.9}O_3$ composite ceramics, Compos. Part B Eng. 166 (2019) 204–212. https://doi.org/10.1016/j.compositesb.2018.12.010.

[43] R. Gao, Z. Wang, G. Chen, X. Deng, W. Cai, C. Fu, Influence of core size on the multiferroic properties of $CoFe_2O_4$@$BaTiO_3$ core shell structured composites, Ceram. Int. 44 (2018) S84–S87. https://doi.org/10.1016/j.ceramint.2018.08.234.

[44] R. Gao, X. Qin, Q. Zhang, Z. Xu, Z. Wang, C. Fu, G. Chen, X. Deng, W. Cai, Enhancement of magnetoelectric properties of $(1-x)Mn_{0.5}Zn_{0.5}Fe_2O_{4-x}Ba_{0.8}5Sr_{0.15}Ti_{0.9}Hf_{0.1}O_3$ composite ceramics, J. Alloys Compd. 795 (2019) 501–512. https://doi.org/10.1016/j.jallcom.2019.05.013.

[45] M.N. Palatnikov, V.A. Sandler, N. V. Sidorov, O. V. Makarova, I. V. Biryukova, I.N. Efremov, D. V. Ivanenko, Spontaneous unipolarity and anomalies of the dielectric and piezoelectric properties and electrical conductivity of initially heavily doped polydomain LiNbO3: Zn crystals, Phys. Solid State. 57 (2015) 1541–1546. https://doi.org/10.1134/S1063783415080235.

[46] M.N. Palatnikov, V.A. Sandler, N. V. Sidorov, I. V. Biryukova, O. V. Makarova, Electrical Conductivity and Dielectric Permittivity of Directly Doped $LiNbO_3$:Zn,Mg Crystals in the Temperature Range 450–900 K, Inorg. Mater. 56 (2020) 955–961. https://doi.org/10.1134/S0020168520080129.

[47] M.N. Palatnikov, N. V. Sidorov, O. V. Makarova, I. V. Birjukova, Features of the Postgrowth Thermal and Electrothermal Treatment of Nominally Pure and Heavily Doped Lithium–Niobate Crystals, Bull. Russ. Acad. Sci. Phys. 82 (2018) 314–316. https://doi.org/10.3103/S1062873818030176.

[48] M.N. Palatnikov, V.A. Sandler, N. V. Sidorov, O. V. Makarova, Anomalous dielectric and piezoelectric properties and electrical conductivity of heavily doped LiNbO3:Zn crystals, Inorg. Mater. 52 (2016) 147–152. https://doi.org/10.1134/S0020168516020114.

[49] M.N. Palatnikov, V.A. Sandler, O. V. Makarova, N. V. Sidorov, D. V. Manukovskaya, I.N. Efremov, I. V. Biryukova, K. Bormanis, Anomalies of dielectric properties and conductivity in single domain $LiNbO_3$:Zn crystals, Integr. Ferroelectr. 173 (2016) 119–127. https://doi.org/10.1080/10584587.2016.1186431.

[50] M.N. Palatnikov, V.A. Sandler, N. V. Sidorov, I. V. Biryukova, O. V. Makarova, Dielectric and piezoelectric properties and electrical conductivity of $LiNbO_3$:ZnO crystals in a wide range of dopant concentrations, Inorg. Mater. 52 (2016) 1291–1296. https://doi.org/10.1134/S0020168516120086.

[51] S. Banerjee, M. Kumar Bhunia, A. Bhaumik, D. Chakravorty, Multifunctional behaviour of mesoporous $LiNbO_3$, J. Appl. Phys. 111 (2012) 054310. https://doi.org/10.1063/1.3693041.

[52] C.A. Diaz-Moreno, Y. Ding, J. Portelles, J. Heiras, A.H. Macias, A. Syeed, A. Paez, C. Li, J. López, R. Wicker, Optical properties of ferroelectric lanthanum lithium niobate, Ceram. Int. 44 (2018) 4727–4733. https://doi.org/10.1016/j.ceramint.2017.12.055.

[53] H. Wu, Z. Zeng, S. Xing, M. Lan, W. Li, Q. Zhang, H. Ao, C. Zhou, R. Xu, R. Gao, X. Deng, Microstructure, Magnetodielectric, and Multiferroic Properties of $xCo_{0.8}Cu_{0.2}Fe_2O_{4-y}(_{0.8}BaTiO_{3-0.2}BiAlO_3)$ Composite Ceramics, Adv. Eng. Mater. 23 (2021) 1–13. https://doi.org/10.1002/adem.202100410.

[54] H. Wu, W. Li, H. Ao, Z. Zeng, X. Qin, S. Xing, C. Zhou, R. Gao, X. Deng, W. Cai, G. Chen, Z. Wang, X. Lei, C. Fu, Effect of holding time on microstructure, ferroelectric and energy-storage properties of $Pb_{0.925}La0_{.05}Zr_{0.95}Ti_{0.05}O_3@SiO_2$ ceramics, J. Alloys Compd. 896 (2022) 162932. https://doi.org/10.1016/j.jallcom.2021.162932.

[55] H. Wu, R. Xu, C. Zhou, S. Xing, Z. Zeng, H. Ao, W. Li, X. Qin, R. Gao, Effect of core size on the magnetoelectric properties of $Cu0_{.8}Co_{0.2}Fe_2O_4@Ba_{0.8}Sr_{0.2}TiO_3$ ceramics, J. Phys. Chem. Solids. 160 (2022) 110314. https://doi.org/10.1016/j.jpcs.2021.110314.

[56] M.N. Palatnikov, V.A. Sandler, N. V. Sidorov, O. V. Makarova, Evolution of the Domain Structure of $LiNbO_3$:ZnO Crystals during High-Temperature Annealing, Inorg. Mater. 54 (2018) 915–919. https://doi.org/10.1134/S002016851809011X.